PAPER

Check for updates

Molecularly engineered Li compensation agent-integrated separator enabling regeneration of degraded LiFePO4

Fujun Tao, [†a] Zeyi Yao, [†a] Jiahui Hou, [a] Zexin Wang, [a] Zhenzhen Yang [b] and Yan Wang [*a]

Lithium replenishment separators (LRSs) integrating pre-lithiation agents can regenerate degraded lithium cathodes *via* facile reassembly with a fresh anode and the LRS. A persistent challenge is the formation of gas or solid residues during pre-lithiation. To address this, for the first time, we develop an LRS based on a molecularly engineered dilithium salt of tetrafluorohydroquinone, which compensates for lithium loss while generating decomposition products that dissolve in the electrolyte as a favorable additive, without forming gas or solid residues, thus offering a green route for lithium compensation. A pristine $LiFePO_4$‖graphite full cell with the LRS exhibits 9.3% higher overall capacity than a polypropylene separator (PPS) cell after 50 cycles at 0.5C, and the degraded $LiFePO_4$‖graphite full cell incorporating this LRS achieves a 44.9% higher capacity than the PPS-based cell after 200 cycles at 0.5C. Our LRS demonstrates strong potential for high-performance lithium-ion batteries and spent battery regeneration.

1. Introduction

The escalating demand for electric vehicles and portable electronics underscores the urgent need to develop lithium-ion batteries that offer both high energy density and prolonged cycle life.[1–4] The formation of a solid electrolyte interphase (SEI) and the related side reactions on the graphite anode consume 5–20% of lithium from the cathode during the first cycle, leading to substantial initial irreversible capacity loss and decreased lifetime and energy density of lithium-ion batteries.[5–7] To address this challenge, pre-lithiation,[8] which is strategically engineered to offset the initial lithium loss in lithium-ion batteries, represents a conceptually distinct approach from conventional electrode or material pretreatment. This strategy involves the controlled incorporation of additional electrochemically active lithium through designed agents, functionalized materials, or optimized processing before cycling.[9] To date, various pre-lithiation routes have been explored, including chemical[10–12] and electrochemical pre-lithiation,[13,14] direct contact[15] or the external short circuit strategy,[16] as well as the use of pre-lithiation additives in cathodes,[17–19] anodes,[20] separators,[21,22] or electrolytes.[23]

Using pre-lithiation additives has emerged as a promising strategy to mitigate initial irreversible capacity loss in lithium-ion batteries, owing to their facile and safe implementation with a minimal amount of high-capacity agents. In cathode pre-lithiation, the additive undergoes oxidation during charging to release Li^+, which is subsequently incorporated into the anode, thereby compensating for lithium consumption during the initial cycle. Representative additives include ternary $Li_xM_yO_z$ compounds (M = Ni, Co, Fe, *etc.*) such as Li_6CoO_4,[24] Li_5FeO_4,[17] and Li_2NiO_2,[19] binary lithium compounds (*e.g.*, Li_2O_2[25] and Li_3N[26]), and lithium-containing salts such as $Li_2C_4O_4$,[22] $Li_2C_2O_4$,[18] and $Li_2C_3O_5$.[27] Nevertheless, the decomposition of these compounds frequently generates gaseous byproducts, which impede charge transport, compromise cathode integrity, and degrade electrochemical performance. To suppress gas evolution, conversion-type nanocomposites such as M/Li_2O,[5] M/LiF,[7] and M/Li_2S[6,21] (M = Ni, Co, Fe, *etc.*) have been developed. However, these materials introduce substantial pre-lithiation-derived solid residues, which reduce practical energy density and limit their applicability. For example, the decomposition of Co/Li_2O results in the formation of Co_3O_4 as a solid residue.[5] In addition, inorganic lithium compounds, including Li_2S,[28] Li_2Se,[29] and Li_3P[30] have been explored to suppress gas evolution during de-lithiation; nevertheless, the resulting solid residues of S,[28] Se,[29] or P[30] in the cathode similarly limit their practical deployment.

Inspired by cathode pre-lithiation, an *in situ* lithium compensation strategy based on a LRS has recently emerged as a promising approach,[21,31] owing to its simplicity and operational advantages. Unlike cathode pre-lithiation, which may induce material compatibility issues, processing challenges, and pore formation in the electrode, the LRS physically

aDepartment of Material Science and Engineering, Worcester Polytechnic Institute, 100 Institute Rd, Worcester, MA 01609, USA. E-mail: yanwang@wpi.edu

bChemical Sciences and Engineering Division, Argonne National Laboratory, 9700 S Cass Ave, Lemont, IL 60439, USA

† These authors contributed equally to this work.

12314 | *J. Mater. Chem. A*, 2026, **14**, 12314–12324

This journal is © The Royal Society of Chemistry 2026

separates the pre-lithiation agent from the cathode, preserving the electrode's structural integrity after its decomposition.[32] In addition, the conductive LRS can function as a secondary current collector,[32] enhancing electron transport and improving the utilization of active materials, thereby boosting the electrochemical performance of lithium-ion batteries[32] or sodium-ion batteries.[32,33] Moreover, the LRS can be directly applied to regenerate degraded cathodes, such as $LiFePO_4$ (LFP).[34–36] Specifically, degraded cathodes harvested from spent lithium-ion batteries can be reassembled with the LRS and a fresh anode. Unlike conventional recycling approaches,[37,38] which require separation of active materials from the aluminum current collector, this strategy allows direct reassembly of the degraded cathode, bypassing the separation step. Upon initial charging to a predetermined voltage, the pre-lithiation agent in the LRS decomposes, restoring the cell capacity relative to the spent battery. This approach reduces recycling costs while providing a practical and environmentally friendly method for cathode regeneration in spent lithium-ion batteries.[34–36]

While significant efforts have been devoted to developing novel pre-lithiation agents and methods to compensate for the active lithium loss, the gas production[22,32,34–36] and solid residues[5–7,21,28–30] arising from the decomposition of the pre-lithiation agents inhibit the practical application. In this work, we first report an LRS that produces neither gas nor solid residues during the pre-lithiation process, prepared with a molecularly engineered pre-lithiation agent, lithium 2,3,5,6-tetrafluorobenzene-1,4-bis(olate) (LTFBB), directly coated on a commercial PPS. Using a pristine LFP electrode, the LFP‖Gr full cell with the LRS exhibits a 9.3% higher overall capacity than the cell with a PPS after 50 cycles at 0.5C. For degraded LFP (D-LFP) batteries, the D-LFP‖Gr full cell incorporating the LRS achieves a 44.9% higher overall capacity compared to the PPS-based cell after 200 cycles at 0.5C. Furthermore, the decomposition product tetrafluoro-1,4-benzoquinone (TFBQ) of LTFBB dissolves in the electrolyte without generating gas or solid residues, avoiding common side effects associated with conventional designs. This LRS suppresses gas and solid residue formation during the pre-lithiation process, offering new opportunities in this field and demonstrating potential for industrial application.

2. Results and discussion

2.1 Direct regeneration strategy for degraded LFP using an LRS

The LRS-enabled regeneration of degraded LFP and its operational mechanism are schematically depicted in Fig. 1. The lithium compensation agent is coated onto one side of the commercial PPS to fabricate the LRS. Subsequently, the degraded LFP electrode is reassembled into a regenerated battery with a fresh graphite anode, simultaneously replacing the commercial PPS with the LRS (Fig. 1a). During the initial charging process, the high-capacity lithium compensation agent decomposes over a specific voltage range, releasing additional Li^+ ions that can be inserted into the lattice of the LFP cathode during discharge

(Fig. 1b). Consequently, after the initial cycle, the degraded LFP can theoretically be restored, allowing the regenerated Li-ion battery to recover its original capacity.

2.2 Synthesis and characterization of LTFBB

In a previous study,[39] a 4-fluoro-1,2-dihydroxybenzene lithium salt, based on a catechol (1,2-dihydroxybenzene) scaffold, was employed as a multifunctional Li-compensation molecule. Fluorination of the catechol backbone facilitated the formation of a robust cathode/anode electrode interfaces (CEI/SEI) on the electrode surface, contributing to stable long-term cycling performance.[39] Catechol is known to be more prone to oxidation than hydroquinone under ambient conditions.

Here, an air-stable hydroquinone (1,4-dihydroxybenzene) scaffold is employed to construct a molecularly engineered lithium compensation agent. As shown in Fig. 2a, the dilithium salt of tetrafluorohydroquinone (TFHQ) is synthesized via LiH-mediated deprotonation of TFHQ in tetrahydrofuran (THF) at room temperature over 24 h, yielding para-diolate $C_6F_4(OLi)_2$ (LTFBB; Fig. S1). This reaction can be interpreted in terms of Lewis acid–base theory,[39–41] with LiH acting as a Lewis base by donating electron pairs and the hydroxyl groups in TFHQ serving as Lewis acids by accepting electrons through their oxygen atoms. Deprotonation generates two alkoxide intermediates (–OLi) and facilitates coordination of additional lithium ions, producing LTFBB, a stabilized dilithium salt in which both Li^+ ions are effectively coordinated. Each LTFBB unit provides two lithium ions, while the four fluorine substituents exert strong inductive electron-withdrawing effects, finely tuning delithiation and oxidation potentials and enhancing chemical stability.[42–44] Upon charging, LTFBB is oxidized to release Li^+, compensating for active lithium loss and sustaining capacity during prolonged cycling. Furthermore, as reported in previous studies,[39–41] the –OLi intermediates are converted into quinone through oxidation. Consequently, LTFBB is converted into TFBQ, which dissolves in the electrolyte and acts as a stabilizing additive.[45,46]

The as-prepared LTFBB exhibited a hierarchical micro–nano structure, in which the micron-sized secondary particles observed in Fig. 2b are assembled from both nano- and micron-sized primary particles (Fig. S1b). As shown in Fig. 2c, the position and intensity of the characteristic peaks in the powder X-ray diffraction (XRD) patterns changed significantly between TFHQ and LTFBB, indicating distinct crystal structures and confirming the formation of a new compound. The Fourier Transform Infrared (FTIR) spectra of LTFBB and TFHQ are shown in Fig. 2d. The disappearance of peaks in the 3000–3500 cm^{-1} range after the transformation from TFHQ to LTFBB suggests that the hydrogen atoms of the hydroxyl groups were replaced by lithium.[39,41] Inductively Coupled Plasma-Optical Emission Spectroscopy (ICP-OES) was used to determine the Li content of TFHQ and LTFBB. As shown in Fig. 2e, LTFBB exhibits a Li content of 7.14% (Table S1), approaching the theoretical value of 7.2% (Table S2). Moreover, the Energy-Dispersive X-ray Spectroscopy (EDS) results in Fig. S2 show an F : O weight ratio of 2.15, which is close to the theoretical ratio
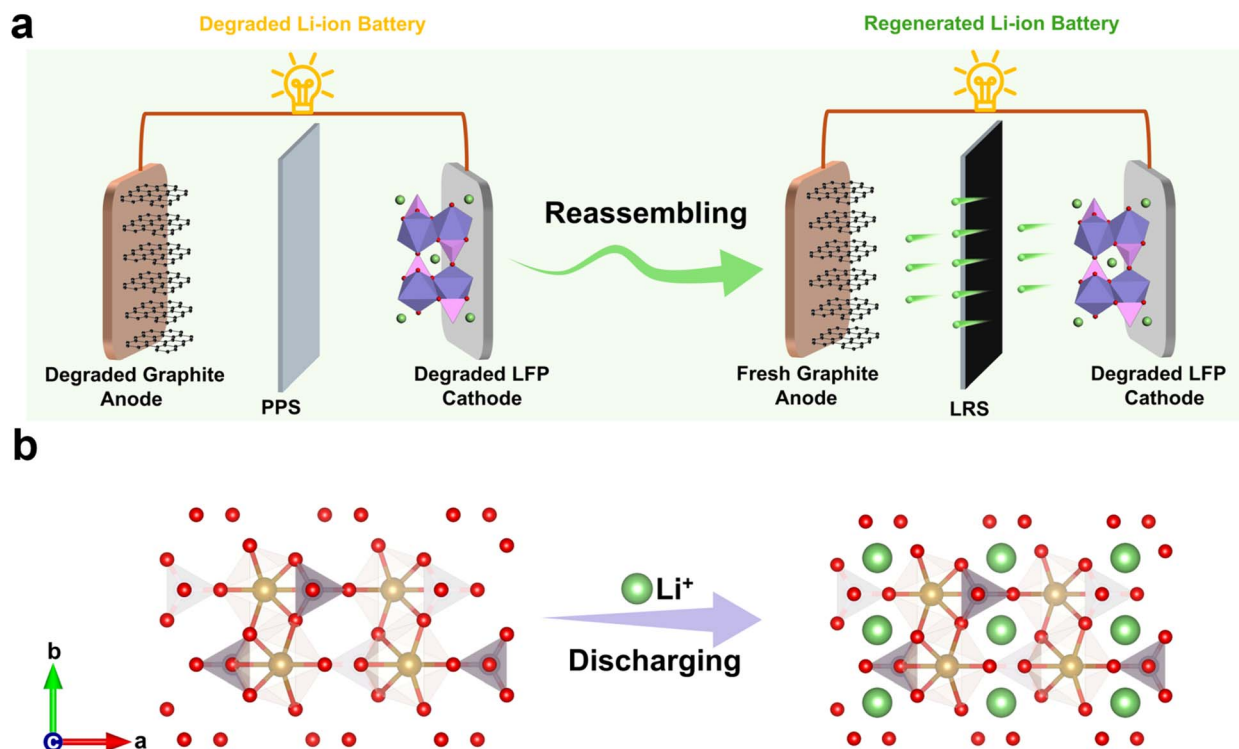
This journal is © The Royal Society of Chemistry 2026

J. Mater. Chem. A, 2026, 14, 12314–12324 | 12315

Fig. 1 Schematic illustration of (a) the direct regeneration strategy for degraded LFP batteries using the LRS and (b) Li$^+$ intercalation into the LFP cathode during discharge.

of 2.38, indicating that the as-synthesized LTFBB is essentially of high purity. X-ray photoelectron spectroscopy (XPS) elemental analysis was used to identify TFHQ and LTFBB. Furthermore, the Li 1s signal is observed for LTFBB in the XPS spectrum, whereas no corresponding signal is detected in the TFHQ spectrum (Fig. S3a). For LTFBB, a distinct and symmetric Li–O peak appears at approximately 56.4 eV (Fig. S3a and b), consistent with those reported for other lithium-containing organic compounds.[39,40]

The electrochemical performance of LTFBB was evaluated by cyclic voltammetry (CV). Material conductivity plays a critical role in determining electrochemical behavior. For instance, highly conductive GeP$_5$ (ref. 47) delivers exceptional reversible capacity, whereas poorly conductive Si[48] exhibits low utilization. For LTFBB, its low conductivity is expected to hinder delithiation. To investigate this effect, three conductive additives, namely Super C65, Super C65 & mesoporous carbon (CMK), and carbon black-ketjenblack EC-600JD (KB), were employed to assess their impact on the delithiation potential. As shown in Fig. S4a, the CV profile of LTFBB with Super C65 exhibits two pronounced anodic peaks at approximately 3.7 and 4.64 V, extending to about 4.75 V, corresponding to Li$^+$ extraction. A weak cathodic peak suggests that lithium removal is largely irreversible. In the second cycle, both anodic and cathodic features persist but are markedly diminished, indicating that most capacity loss occurs in the first cycle. Galvanostatic charge–discharge measurements corroborate this observation, revealing a charge-specific capacity of 200.3 mA h g^{-1} at 4.75 V, while the capacity is only 57.6 mA h g^{-1} at 4.3 V (Fig. S4b). This

is significantly higher than the typical operating voltages of commercial cathodes such as LFP and lithium nickel cobalt manganese oxide (NCM), which are below 4.3 V.[18]

To enhance conductivity, LTFBB was combined with CMK in THF under an argon atmosphere to produce an LTFBB & CMK composite, which was further mixed with Super C65 for electrode preparation. The corresponding CV curve (Fig. S5a) shows a slight shift of the main anodic peak from 4.64 to approximately 4.59 V, with capacities of 261.5 and 68.5 mA h g^{-1} at 4.75 and 4.3 V (Fig. S5b), respectively, which are slightly higher than those obtained with Super C65 alone. When KB was used, the CV curve (Fig. 2f) displayed a reduced anodic peak at about 4.5 V, extending to approximately 4.65 V. The corresponding charge–discharge profiles (Fig. 2g) deliver a charge capacity of 273.2 mA h g^{-1} at 4.65 V, which is close to the theoretical specific capacity of 276.3 mA h g^{-1}, and a charge capacity of 150.3 mA h g^{-1} at 4.3 V, with a corresponding discharge capacity of approximately 81.8 mA h g^{-1}. The irreversible primary capacity of LTFBB demonstrates its suitability as a pre-lithiation additive. Compared with Super C65 and Super C65 & CMK, Fig. S6 demonstrates that KB as a conductive additive delivers the highest charge capacity at 4.3 V, indicating its strong potential for application in commercial cathode systems. Our findings are consistent with the previous report.[18] Using KB as the conductive additive enables the prelithiation agent to exhibit a higher capacity and a lower delithiation potential.[18] This improvement arises from the large specific surface area (~1180 m^2 g^{-1}) of KB,[18] which allows it to embed with LTFBB and form a more efficient electronically conductive network.

12316 | J. Mater. Chem. A, 2026, 14, 12314–12324

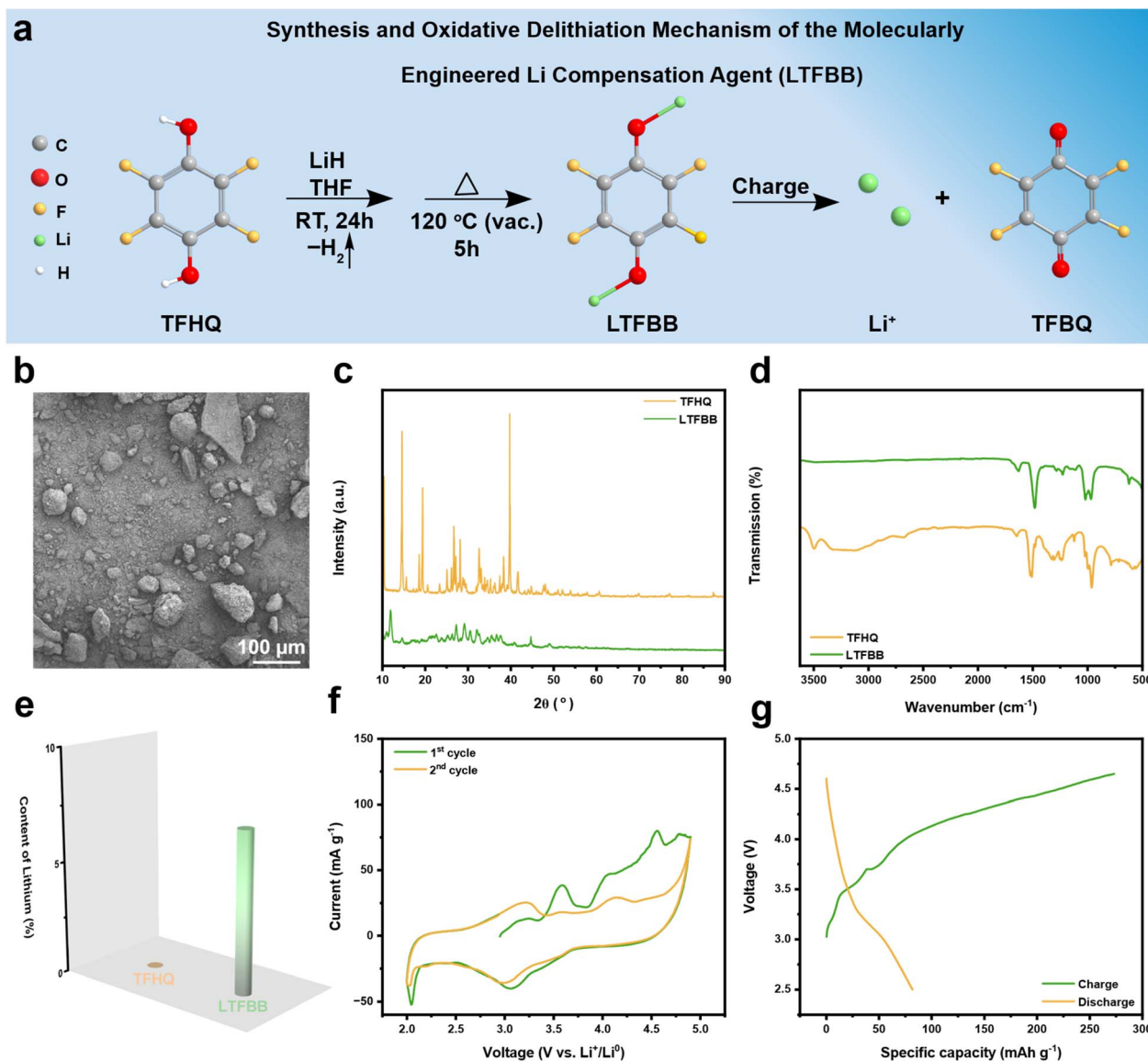This journal is © The Royal Society of Chemistry 2026

Fig. 2 (a) Schematic illustration of the synthesis of LTFBB from TFHQ and its oxidation to TFBQ. (b) SEM image of the as-synthesized LTFBB. (c) PXRD patterns and (d) FTIR spectra of TFHQ and LTFBB. (e) Lithium content of as-synthesized LTFBB by ICP. (f) CV curves of the first and second cycles, and (g) galvanostatic charge–discharge profiles of the LTFBB electrode.

Moreover, the high intrinsic conductivity of KB further facilitates charge transfer. Impressively, LTFBB retains 92.2% of its capacity (*i.e.*, 251.8 mA h g^{-1}) after 24 h of exposure to air at 50% relative humidity (RH) (Fig. S7), indicative of its high air stability. To further investigate the decomposition of LTFBB, we used ICP to determine the Li content of the LTFBB electrode after charging to 4.3 V. As shown in Fig. S8 and Table S3, about 3.12% of Li content remains in LTFBB, indicating that ~56.3% of Li^+ was extracted from the electrode and that LTFBB decomposed during charging. These results demonstrate that LTFBB can serve as an effective pre-lithiation agent.

2.3 Characterization and electrochemical performance of the LRS

To verify the feasibility of using LTFBB as a pre-lithiation agent and to enable a facile pre-lithiation process, we coated it onto

a commercial PPS as a functional layer to prepare the LRS, which served as an additional lithium source in the batteries. As shown in the insets of Fig. 3a, b and S9, the two sides of the LRS exhibit distinct appearances. The lithium-replenishment layer (LTFBB-coated side, the inset of Fig. 3a) appears black due to the uniform distribution of LTFBB and KB, whereas the opposite side (back side, the inset of Fig. 3b) retains the original smooth appearance of the separator. SEM imaging reveals multiple cracks on the coated side (Fig. 3a), originating from the high porosity of the KB conductive carbon network. The corresponding inset (Fig. 3a) further displays a coarse, granular morphology resulting from the LTFBB–KB coating. In contrast, the backside retains the original smooth surface of the separator, with no penetration of coating particles detected at the microscopic level (Fig. 3b), confirming that the separator's insulating properties remain unaffected. The XRD patterns

This journal is © The Royal Society of Chemistry 2026

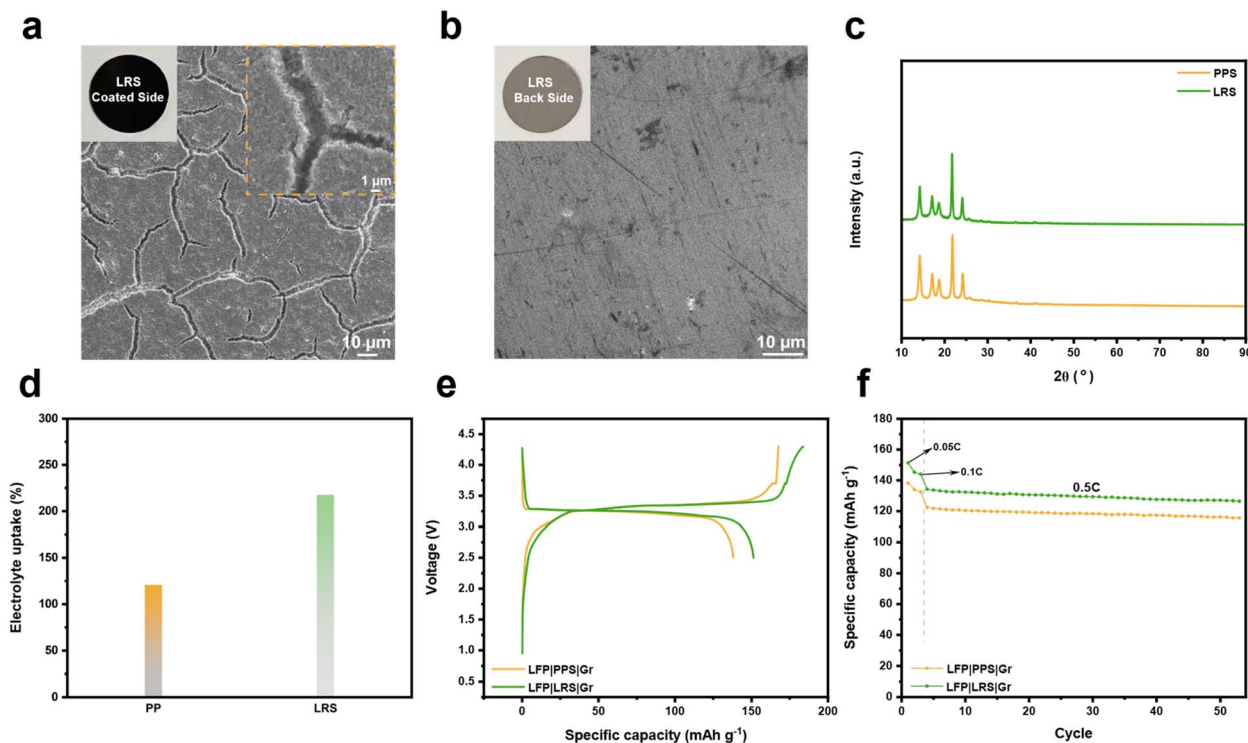J. Mater. Chem. A, 2026, **14**, 12314–12324 | **12317**

Fig. 3 (a) SEM image and an optical photo (inset) of the LTFBB-coated sides of the as-prepared LRS. (b) SEM image and an optical photo (inset) of the backside of the as-prepared LRS. (c) XRD patterns of the PPS and LRS. (d) The electrolyte uptake capacity of the PPS and LRS. Electrochemical performance of pristine LFP∥Gr full cells with the LRS and PPS. (e) Initial charge/discharge profiles at 0.05C. (f) Cycling performance at 0.5C.

(Fig. 3c) of the PPS and LRS in the 10–90° range and the zoomed region (Fig. S10) from 25° to 40° show no appreciable differences, as the peaks corresponding to the LTFBB loading are likely obscured by those of the PPS. XPS analysis was then performed to examine the chemical state of LTFBB after coating onto the PPS. A distinct Li–O peak at ∼56.4 eV (Fig. S11) indicates that the local chemical environment of lithium is largely preserved during the coating process. The wettability of the PPS and LRS toward the LP57 electrolyte is shown in Fig. S12. The contact angles of the PPS and LRS are 59 ± 1° and 18 ± 1°, respectively. The significantly lower contact angle of the LRS indicates its superior electrolyte wettability. Fig. 3d presents the electrolyte absorption behavior of the LRS. After being fully immersed in LP57 electrolyte, the LRS exhibits markedly enhanced electrolyte uptake capacity compared with the PPS. This enhancement is attributed to the lithium compensation agent coating with high specific surface area KB on the PPS, enabling the LRS to achieve an electrolyte uptake of ∼217%, significantly higher than the ∼121% observed for the PPS. Furthermore, the LRS exhibited a higher porosity of 79.5% compared to 45% for the PPS (Fig. S13). The increased electrolyte uptake and porosity may enhance ion transport. As shown in Fig. S13, the LRS shows a higher ionic conductivity of 1.23 mS cm^{-1}, compared to 0.55 mS cm^{-1} for the PPS.

Active lithium loss during the initial cycle substantially reduces the energy density of lithium-ion batteries. To address this issue, a LRS was employed as an external lithium source to compensate for the initial lithium loss, providing a straightforward strategy for lithium replenishment.[21,22,32] The electrochemical performance of the LRS was evaluated in full cells comprising fresh LFP as the cathode and graphite as the anode. Fig. S14 presents the initial charge–discharge profiles of pristine LFP∥Gr full cells with the PPS or LRS loaded with ∼0.15 mg cm^{-2} LTFBB. The LRS-equipped cell exhibits higher initial charge and discharge capacities than the conventional PPS cell (Fig. S14a). Specifically, the PPS cell delivers a charge capacity of 167.7 mA h g^{-1} and a discharge capacity of 138.1 mA h g^{-1}, whereas the LRS-containing cell achieves a charge capacity of 176.5 mA h g^{-1} and a discharge capacity of 146.3 mA h g^{-1}, corresponding to increases of 8.8 and 8.1 mA h g^{-1}, respectively. This improvement is ascribed to the effective compensation of initial lithium loss by LTFBB. The LRS cell further demonstrates enhanced cycling stability, retaining 6% higher capacity than the PPS cell after 50 cycles at 0.5C (Fig. S14b). Charge–discharge profiles (Fig. S14c and d) collected at 0.05C, 0.1C, and 0.5C throughout cycling indicate that the capacity enhancement of the LRS persists across all tested current rates. Upon increasing the LTFBB loading on the LRS to ∼0.3 mg cm^{-2}, the benefits of the LRS are further amplified. The corresponding full cell delivers a charge capacity of 183.8 mA h g^{-1} and a discharge capacity of 151.3 mA h g^{-1}, representing improvements of 16.1 and 13.2 mA h g^{-1} relative to the PPS cell (Fig. 3e). The LRS-equipped cell also exhibits superior cycling performance, retaining 9.3% higher capacity than the PPS cell after 50 cycles at 0.5C (Fig. 3f). Compared with the PPS (Fig. S14d), charge–discharge profiles collected at 0.05C, 0.1C, and 0.5C during the 50th cycle (Fig. S15) indicate that the LRS consistently enhances both charge and discharge
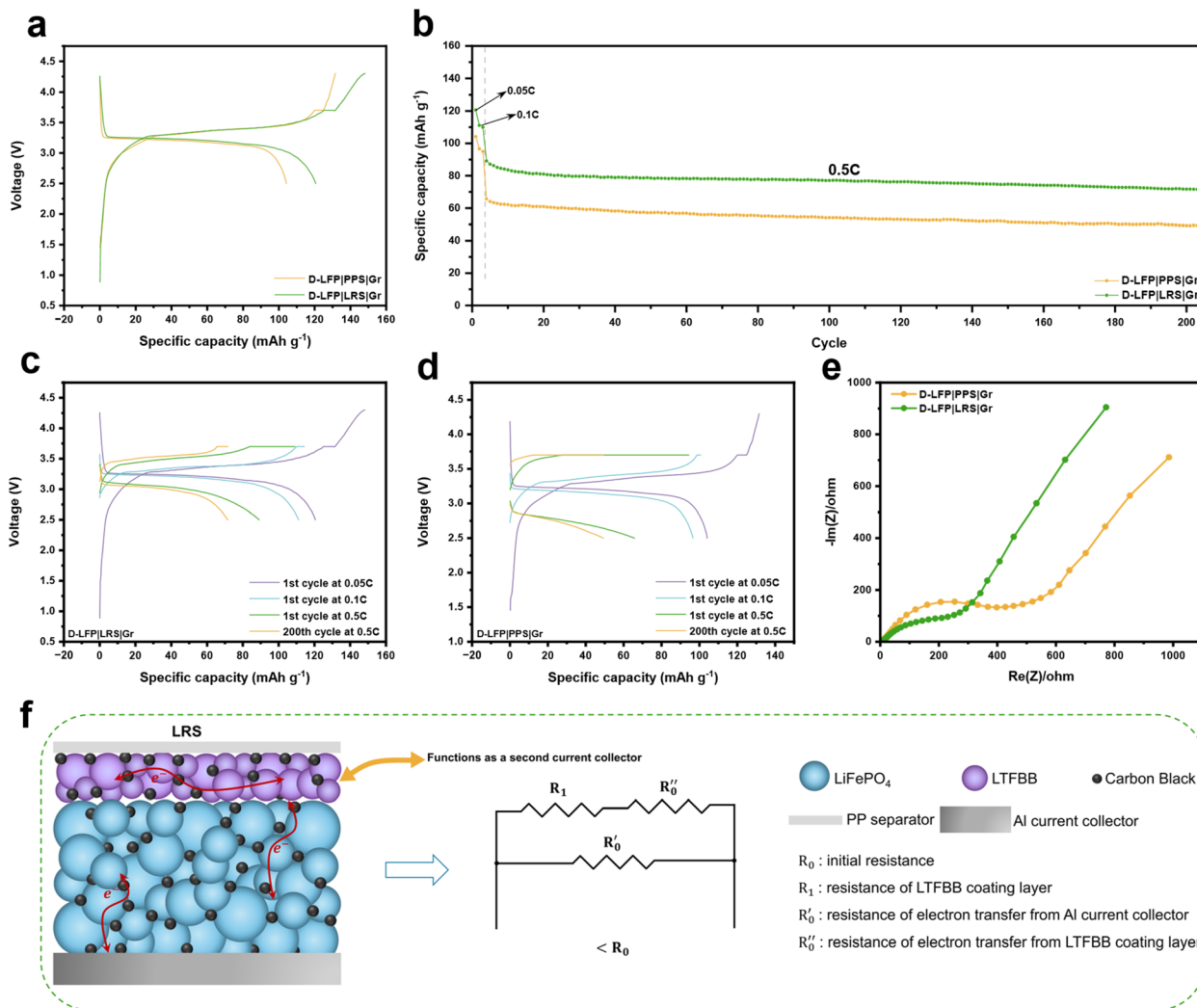
12318 | J. Mater. Chem. A, 2026, 14, 12314–12324

This journal is © The Royal Society of Chemistry 2026

Fig. 4 Electrochemical performance of D-LFP‖Gr full cells with the LRS and PPS. (a) Initial charge/discharge profiles at 0.05C. (b) Cycling performance. Charge−discharge profiles of D-LFP‖Gr full cells with (c) LRS and (d) PPS, respectively, at various cycles. (e) EIS for the D-LFP‖Gr full cells with the LRS and PPS after formation. (f) Effect of the LRS on resistance.

capacities across all tested current rates. The coulombic efficiency (Fig. S16) remains nearly unchanged for both the PPS cell and LRS cells, suggesting that the capacity improvement in the LRS cell mainly originates from the additional lithium supplied to the cell. Furthermore, the XRD patterns (Fig. S17a) of the pristine LRS and cycled LRS remain nearly unchanged. Moreover, the LRS retains an identical morphology before (Fig. 3a) and after cycling (Fig. S17b), demonstrating that the functionalization preserves its structural integrity upon delithiation.

2.4 Electrochemical evaluation of the regeneration strategy using the LRS

The promising capacity-enhancing effect of the LRS in fresh LFP‖Gr full cells motivated us to investigate its impact on D-LFP electrodes. We examined the electrochemical performance of full cells based on a D-LFP cathode and fresh graphite anode with or without the LRS. As shown in Fig. 4a, the initial charge capacity of the D-LFP‖Gr full cell is only 131.6 mA h g^{-1} and the corresponding discharge capacity is 104.5 mA h g^{-1} at 0.05C,

likely due to lithium loss, oxidation of the LFP electrode, or other degradation mechanisms. In contrast, the regenerated cell incorporating the LRS with ∼0.4 mg cm^{-2} LTFBB achieves a significantly higher initial charge capacity of 148.2 mA h g^{-1}, attributed to Li$^+$ compensation from the decomposition of LTFBB. The additional lithium supplied by LTFBB restores the discharge capacity of D-LFP to 120.6 mA h g^{-1}. After 200 cycles at 0.5C (Fig. 4b), the regenerated cell exhibits a 44.9% capacity improvement compared to the cell with the conventional PPS. Specifically, the LRS-based regenerated cell reaches 71.6 mA h g^{-1}, whereas the PPS-based cell delivers 49.4 mA h g^{-1}. Furthermore, the LRS-based cell (Fig. 4c) retains higher charge/discharge capacities than the PPS-based cell (Fig. 4d) across increasing rates of 0.05C, 0.1C, and 0.5C. Electrochemical impedance spectra (EIS) of LRS and PPS cells after formation (Fig. 4e and S18) reveal that the LRS cell has lower resistance, possibly due to enhanced electron transfer facilitated by the conductive separator acting as a secondary current collector (Fig. 4f) compared with the PPS (Fig. S19). This

LRS could promote more efficient electron transport and active material utilization, leading to reduced resistance and improved capacity recovery.[32]

Increasing the LTFBB loading on the LRS to ~0.65 mg cm^{-2} (Fig. S20) increases the charge and discharge capacities to 160.7 and 126.7 mA h g^{-1}, respectively. After 100 cycles at 0.5C, the regenerated cell shows a 51% capacity improvement over the PPS-based cell. Further increasing the LTFBB loading to ~1 mg cm^{-2} (Fig. S21) boosts the charge and discharge capacities to 172.4 and 131.3 mA h g^{-1}, respectively. However, excessive LTFBB loading on the LRS may bring adverse effects to the battery, causing faster capacity fade at 0.5C. As shown in Fig. S22a, the PPS clearly exhibits its internal pores. In comparison, the main part (Fig. S22b and c) of the LTFBB coating on the LRS with ~1.0 mg cm^{-2} LTFBB loading not only covers the LRS pores, but the cracked regions (Fig. S22d) of the LRS also cover the pores of the PPS. With increasing LTFBB loading (*i.e.*, thicker coating), more nano- to micro-sized particles accumulate on the separator, which increases the ion

transport path and likely causes the capacity decay observed in the LRS at high LTFBB loadings. Besides, the ionic conductivity of the LRS (Fig. S23) decreases from 1.703 mS cm^{-1} for ~0.4 mg cm^{-2} LTFBB to 1.108 mS cm^{-1} for ~1.0 mg cm^{-2} LTFBB, reflecting the hindered ion transport caused by the thicker LTFBB coating.

Although the D-LFP cell could not be fully restored to its ideal capacity due to the limited LTFBB capacity in the voltage window (≤4.3 V), restricted LTFBB loading, and the inability of Li$^+$ to intercalate into degraded LFP electrodes, the results demonstrate the effectiveness of *in situ* electrochemical regeneration for D-LFP electrodes. The capacity fading of D-LFP may arise from cycling-induced micro-cracks in larger LFP grains,[49,50] loss of crystallinity and the active material,[49,51] and carbon aggregation and agglomeration.[52–54] As shown in Fig. S24, the (002) plane of conductive carbon is observed in the XRD pattern of the degraded LFP electrode, whereas it is absent in fresh LFP powder and fresh LFP electrodes. This carbon peak likely originates from carbon aggregation, which further leads
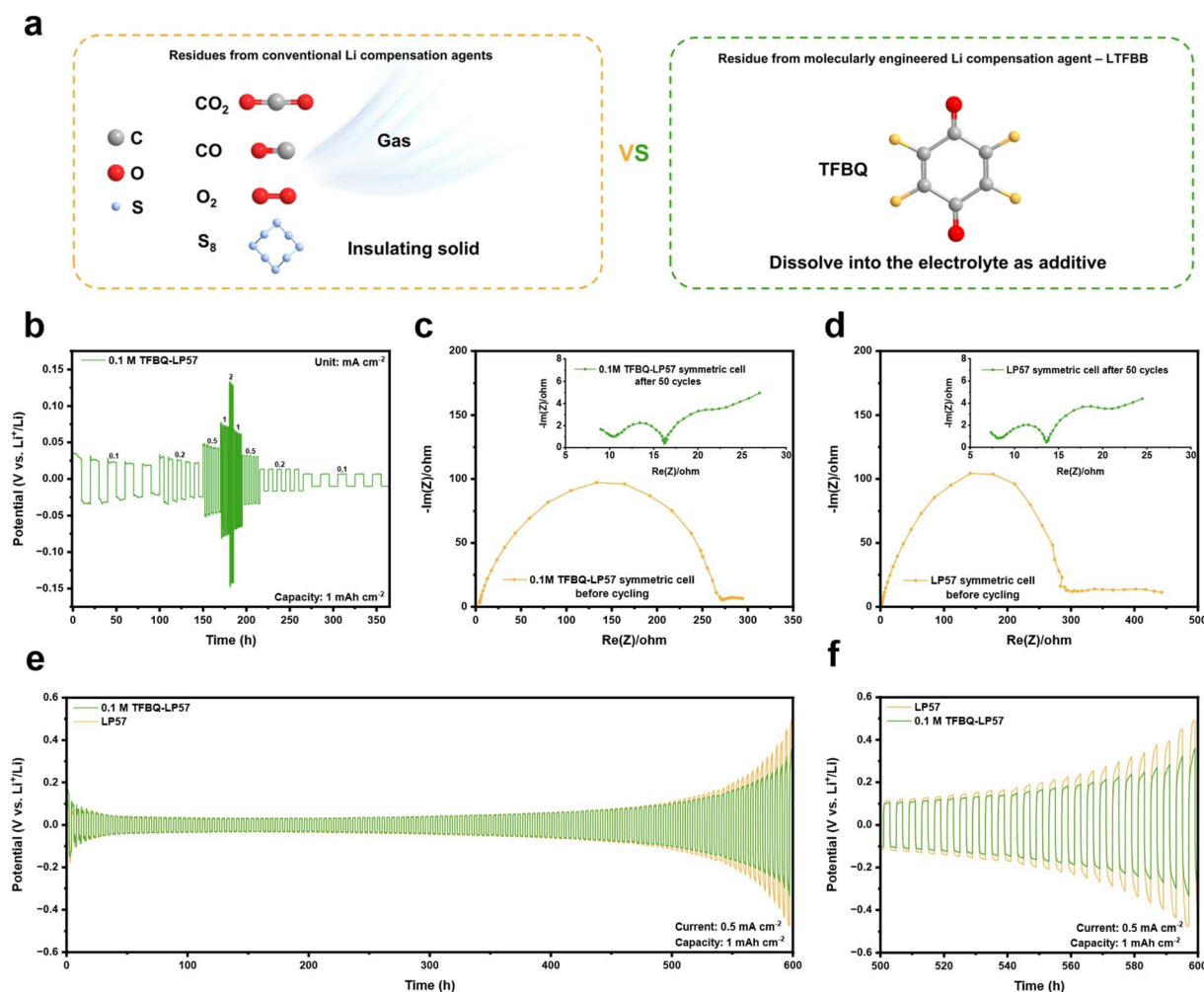

Fig. 5 (a) Comparison of residues from conventional and molecularly engineered Li compensation agent. (b) Galvanostatic rate performance of the 0.1 M TFBQ–LP57 symmetrical cell at various densities (0.1–2 mA cm^{-2}) and with a capacity of 1 mA h cm^{-2}. Nyquist plots of the impedance spectra of (c) 0.1 M TFBQ–LP57 and (d) LP57 symmetrical cells, before and after (inset) the first 50 cycles. Galvanostatic cycling performance of 0.1 M TFBQ–LP57 and LP57 symmetrical cells at 0.5 mA cm^{-2}/1 mA h cm^{-2} for (e) 600 h, with a zoomed-in view from (f) 500 to 600 h.

12320 | *J. Mater. Chem. A*, 2026, **14**, 12314–12324

This journal is © The Royal Society of Chemistry 2026

to a reduction in the effective active material and consequently inhibits the capacity recovery of the D-LFP electrodes during the prelithiation process. This strategy provides a promising route for directly regenerating degraded electrodes *via* the LRS by incorporating a molecularly engineered Li compensation agent with high theoretical specific capacity, which merits further exploration.

2.5 Electrochemical evaluation of the byproduct of the LRS

Compared with previously reported conventional LRSs, which often generate gaseous products (*e.g.*, CO_2,[34] CO,[32] and O_2 (ref. 36)) or solid residues (*e.g.*, S_8)[28] during cycling (Fig. 5a), the developed LRS based on LTFBB operates without gas evolution or solid by-products. Notably, the reaction by-product TFBQ is highly soluble in ether- and ester-based electrolytes.[45] On the anode of the LFP‖Gr full cell, similar to the previous report,[39] the by-product TFBQ participates in the redox reaction, during which the C–F bonds are cleaved, and the released F^- combines with Li^+ to form LiF while generating C=O functionalities.[45] As shown in Fig. S25a and b, the F 1s XPS spectrum reveals a higher LiF content in the LRS-cycled cell (~98.8%) compared with the PPS-cycled cell (~73.7%). This increased LiF content contributes to reinforcing the SEI and mitigating lithium dendrite formation.[39,45,55] Furthermore, increased C=O groups are observed in the LRS-cycled cell, as indicated by the C 1s (Fig. S25c and d) XPS spectra (~19.2% *vs.* ~14.3%). These C=O groups enhance ionic conduction at the electrolyte–electrode interface, while their higher bond energy helps suppress electrolyte oxidation.[39]

Furthermore, lithium metal batteries offer ultrahigh energy density owing to the high capacity and low redox potential of lithium metal anodes, but their practical application is hindered by severe lithium dendrite growth and poor cycling stability.[56] In our previous work,[45] TFBQ showed high solubility in 1,3-dioxolane (DOL)/1,2-dimethoxyethane (DME) with lithium bis(trifuoromethanesulfonyl)imide (LiTFSI) electrolyte and improved cell stability and cycle life in lithium metal batteries by suppressing lithium dendrite formation on the anode. Moreover, TFBQ is also well soluble in the LP57 electrolyte (Fig. S26), which is the base electrolyte employed in this work. As shown in Table S4, the concentration of TFBQ generated during the LTFBB decomposition in the electrolyte was ~7.46, 14.9, 19.9, 32.7, and 50.1 mM for the LRS with LTFBB loadings of ~0.15, 0.3, 0.4, 0.65, and 1 mg cm^{-2}, respectively. And following our previous work,[45] 0.1 M TFBQ was added to LP57 to prepare the 0.1 M TFBQ–LP57 electrolyte. As shown in Fig. 5b, the Li–Li symmetrical cell with 0.1 M TFBQ–LP57 exhibits potentials of ~22/25/46/75/138/64/34/16/10 mV at current densities of 0.1/0.2/0.5/1/2/1/0.5/0.2/0.1 mA cm^{-2}, respectively. In comparison, the cell with LP57 shows lower polarization, with potentials of ~22/23/37/56/92/48/28/14/9 mV under the same conditions (Fig. S27), indicating that the presence of TFBQ slightly increases overpotential. The initial interfacial resistance of the cell with 0.1 M TFBQ–LP57 after 24 h of rest is relatively large (Fig. 5c) but decreases to ~20 Ω after 50 cycles (inset of Fig. 5c and S28a), which is comparable to

that of the LP57 cell (inset of Fig. 5d and S28b). At a current density of 0.5 mA cm^{-2} and capacity of 1 mA h cm^{-2}, the Li–Li symmetrical cell with 0.1 M TFBQ–LP57 exhibits a higher potential than the LP57 cell during the first 50 cycles (Fig. 5e), attributed to the additive and the incomplete formation of the F-rich protective layer on the Li surface. After 500 h, the TFBQ-containing cell clearly exhibits a lower potential than the LP57 cell (Fig. 5f), suggesting that the F-rich protective layer effectively suppresses dendrite growth. A similar trend is observed at a higher current density of 2 mA cm^{-2} (Fig. S29a and b). Notably, from 50 h to 80 h, the cell with 0.1 M TFBQ–LP57 consistently retains a lower overpotential than the LP57 cell. Although TFBQ slightly increases polarization across 0.1–2 mA cm^{-2}, its long-term effect is beneficial, as the cell demonstrates reduced overpotential after 50 h of cycling at 2 mA cm^{-2}. This finding demonstrates a promising approach to utilize molecularly engineered LTFBB as a lithium compensation agent for mitigating active lithium loss in lithium-ion batteries without generating gas or solid byproducts, with residual TFBQ concurrently serving as a stabilizing electrolyte additive.

3. Conclusions

A functional lithium replenishment separator incorporating a molecularly engineered organic lithium compensation agent, LTFBB, has been developed to regenerate D-LFP. LTFBB was synthesized *via* a simple chemical reaction using LiH and TFHQ. The areal mass loading of LTFBB on the PPS can be precisely adjusted, enabling controlled Li^+ release to replenish the capacity of LFP batteries. Consequently, LTFBB exhibited significant effects in compensating for the initial lithium loss when incorporated into a pristine LFP full cell. The pristine LFP full cell with the LRS shows a 9.3% higher capacity than the LFP full cell with the PPS. Impressively, the D-LFP‖Gr full cell incorporating the LRS achieves a 44.9% higher overall capacity than the PPS-based cell after 200 cycles at 0.5C. This as-made molecularly engineered LRS provides a promising and simple regeneration strategy for lithium battery recovery, broadening the horizons of the existing industrial battery recycling process. It is promising to anticipate that increased research efforts on this molecularly engineered strategy-based LRS, which does not produce gaseous products or solid residues in the battery, will contribute to advancing the regeneration of degraded lithium-ion batteries.

4. Methods

4.1 Materials

Tetrafluorohydroquinone (TFHQ), tetrafluoro-1,4-benzoquinone (TFBQ), anhydrous tetrahydrofuran (THF), mesoporous carbon (CMK), N-methyl-2-pyrrolidone (NMP) and isopropyl alcohol (IPA) were purchased from Sigma-Aldrich Corporation. Lithium hydride (LiH) was obtained from Thermo Fisher Scientific. Carbon black-ketjenblack EC-600JD (KB) was provided by the Fuel Cell Store. Super C65 conductive carbon black and LA133 were sourced from MSE supplies. The PP separator (PPS) was procured from Celgard LLC. The

This journal is © The Royal Society of Chemistry 2026

J. Mater. Chem. A, 2026, **14**, 12314–12324 | **12321**

$LiFePO_4$, Gr powder, and polyvinylidene fluoride (PVDF) were acquired from MTI Corporation. The degraded LFP electrode, with a loading of approximately 6 mg cm^{-2}, was supplied by MTI Corporation. Its capacity had degraded to less than 80% of the original capacity and it had been exposed to air for an extended period. All chemicals and solvents were used as received without any further purification.

4.2 Lithium salt synthesis

The lithium salt was synthesized following a previously reported method.[39–41] All preparations were conducted under an argon atmosphere at ambient temperature. 1 mmol of TFHQ was dissolved in 2 mL of anhydrous THF in a glass vial and stirred for 10 minutes to ensure complete dissolution. Subsequently, 2 mmol LiH was introduced to the transparent solution, and the resulting mixture was stirred continuously for 24 hours. The resulting product, lithium 2,3,5,6-tetrafluorobenzene-1,4-bis(olate) (LTFBB), was obtained after being dried under vacuum at 120 °C for 5 hours in an oven.

4.3 Preparation of the LTFBB electrode and LRS

The LTFBB electrodes for cyclic voltammetry (CV) and capacity testing were prepared by mixing LTFBB, conductive carbon, and PVDF binder in a weight ratio of 6 : 3 : 1, using NMP as the solvent. The conductive carbons used were Super C65, a Super C65 & CMK mixture, and KB, respectively. For LTFBB electrodes containing a mixture of Super C65 and CMK conductive carbons, LTFBB and CMK were first mixed in THF inside a glovebox to form the LTFBB & CMK composite, which was then dried in a vacuum oven at 55 °C. This composite was subsequently mixed with Super C65 and PVDF to obtain a final composition of 60% LTFBB, 15% CMK, 15% Super C65, and 10% PVDF. The resulting slurry was cast onto aluminum foil and dried under vacuum at 55 °C for 12 h. The LTFBB electrodes had an areal loading of approximately 1 mg cm^{-2} with a diameter of ~12 mm. The LRS was fabricated by mixing 60 wt% LTFBB, 30 wt% KB, and 10 wt% PVDF in NMP to obtain a homogeneous slurry. The slurry was cast onto the PPS using a doctor blade and subsequently dried in a vacuum oven at 55 °C for 12 h. The LTFBB loading was adjusted by varying the coating thickness with the doctor blade. After drying, the LRS was punched into 16 mm-diameter disks for full-cell assembly. Finally, by adjusting the doctor-blade gap to increase the thickness of the LTFBB coating, lithium replenishment separators (LRSs) with different areal loadings of LTFBB (i.e., ~0.15, 0.3, 0.4, 0.65, and 1 mg cm^{-2}) were prepared.

4.4 Cell assembly

The half and full cells were assembled into 2032-type coin cells in an argon-filled glovebox (H_2O and O_2 < 0.01 ppm). The LTFBB half cells, used for capacity testing, comprised an LTFBB cathode, a PPS, electrolyte, and a lithium metal anode. For the LFP∥Gr full cells, LFP electrodes were prepared by mixing LFP, Super C65 conductive carbon, and PVDF binder in a weight ratio of 90 : 5 : 5 using NMP as the solvent. Graphite electrodes were fabricated by blending graphite powder, Super C65 conductive

carbon, and LA133 binder in a weight ratio of 94 : 2 : 4. The slurries were cast onto aluminum foil (LFP) and copper foil (graphite) and then dried under vacuum at 120 °C for 12 h. The LFP electrodes had an areal loading of approximately 5 mg cm^{-2} with a diameter of ~12 mm, while the graphite electrodes had a loading of approximately 2.7 mg cm^{-2} and a diameter of ~14 mm. The negative-to-positive (N/P) capacity ratio was ~1.1. The electrolyte (LP57) comprised 1 M lithium hexafluorophosphate ($LiPF_6$) dissolved in a 3 : 7 (v/v) mixture of ethylene carbonate (EC) and dimethyl carbonate (DMC), with 70 μL added per coin cell. Cells were assembled in an argon-filled glove box with moisture and oxygen levels maintained below 0.01 ppm. For the LRS-based full cell, the as-prepared LRS was oriented with its coated side facing the LFP cathode. For the Li–Li symmetrical cells, 0.1 M TFBQ–LP57 and pristine LP57 were used as the electrolytes, with 50 μL added to each coin cell.

4.5 Material characterization

Morphological characterization and Energy-Dispersive X-ray Spectroscopy (EDS) analyses were performed using a JEOL 7000F scanning electron microscope. Crystal structures of the LTFBB precursor, LTFBB, and LRS were analyzed by X-ray diffraction (Bruker D8 Advance) with Cu Kα radiation in Bragg–Brentano geometry over a 2θ range of 10° to 90°. Fourier transform infrared spectra were obtained with a Bruker Vertex 70 FTIR spectrometer, and X-ray photoelectron spectroscopy (XPS) was performed using an ULVAC-PHI PHI 5000 VersaProbe II system. The Inductively Coupled Plasma-Optical Emission Spectroscopy (ICP-OES) analyses were performed using a Perkin-Elmer Optima 8000 CROSS FLOW. ICP samples were prepared by either dissolving the materials directly in a 2.0 wt% nitric acid aqueous solution or by dissolving them in aqua regia (a 1 : 3 v/v mixture of concentrated nitric and hydrochloric acids) followed by dilution with 2.0 wt% nitric acid. The contact angle was measured using an optical contact angle goniometer (DataPhysics Instruments/OCA11).

4.6 Calculation methodology

The electrolyte uptake (U, %) of the separator was determined by weighing the separator before and after immersion in the electrolyte for 24 h and calculated using the following equation:[32]

$$U(\%) = \frac{m_{after} - m_{before}}{m_{before}}$$

where m_{before} and m_{after} are the weights of the separator before and after immersion in the electrolyte, respectively.

The porosity of the separator was measured using IPA absorption analysis,[57] which involved determining the dry and wet weights of the separator samples before and after soaking in IPA. The separator samples were soaked in IPA for 1 h. The porosity (ε, %) was calculated according to the following equation:[21,58]

$$\varepsilon(\%) = \frac{m_{after} - m_{before}}{\rho V}$$

12322 | J. Mater. Chem. A, 2026, 14, 12314–12324

This journal is © The Royal Society of Chemistry 2026

where m_{before} and m_{after} are the weights of the separator before and after soaking in IPA, ρ is the density of IPA, and V is the volume of the separator.

The ionic conductivity (σ) of the separator in the electrolyte was measured by electrochemical impedance spectroscopy (EIS) using a stainless-steel symmetric cell. The ionic conductivity was calculated according to the following equation:[22,32]

$$\sigma = \frac{L}{A_s \times R_s}$$

where L denotes the thickness of the separator, A_s is the effective area of the separator, which is equal to the area of the stainless steel electrode, and R_s represents the bulk resistance.

4.7 Electrochemical characterization

Electrochemical tests were performed using a LAND battery testing system at 25 °C. All cells were rested for 24 h prior to testing. The LFP‖Gr full cell was first charged to 3.7 V at 0.05C (1C = 154 mA h g^{-1} for fresh LFP and 1C = 150 mA h g^{-1} for degraded LFP), followed by a constant voltage-constant current (CVC) step, and then charged to 4.3 V at a lower current density of 0.02C to decompose the LTFBB. Capacity testing of the LTFBB electrode was carried out using the same procedure. Rate performance of Li–Li symmetrical cells was evaluated at 0.1, 0.2, 0.5, 1, and 2 mA cm^{-2}, with a fixed capacity of 1 mA h cm^{-2} at each current density, and 0.5 and 2 mA cm^{-2} were selected for cycling tests. CV and electrochemical impedance spectroscopy (EIS) measurements were conducted on an electrochemical analyzer (Bio-Logic SAS VMP3). EIS measurements of LFP‖Gr full cells and Li–Li symmetrical cells were conducted over frequency ranges of 100 kHz to 0.1 Hz and 100 kHz to 0.01 Hz, respectively, with a 10 mV voltage amplitude.

Author contributions

F. Tao and Z. Yao conducted the experiments and wrote the manuscript. J. Hou and Z. Wang performed the ICP measurements. Z. Yang carried out the XPS characterization. Y. Wang supervised this research project.

Conflicts of interest

There are no conflicts to declare.

Data availability

The data supporting this article have been included as part of the supplementary information (SI). Supplementary information: a photo and the SEM image of LTFBB; EDS spectrum of LTFBB; XPS spectra of TFHQ and LTFBB; CV curves of the LTFBB electrode with Super C65 and Super C65 & CMK, respectively; galvanostatic charge–discharge profiles of the LTFBB electrode with Super C65, Super C65 & CMK and KB as the conductive carbon, respectively; photos of the LRS; XRD patterns of the PPS and LRS over the region from 25° to 40°; XPS spectrum of the LRS; electrochemical performance of LFP‖Gr full cells with LRS ∼ 0.15 mg cm^{-2} LTFBB and PPS; charge–discharge profiles of the full cells with LRS ∼ 0.3 mg cm^{-2} LTFBB at various cycles; SEM image of the LRS after cycling; EIS spectra for D-LFP‖Gr full cells with the LRS or PPS after formation; schematic illustration of the effect of the PPS on resistance; electrochemical performance of D-LFP‖Gr full cells with LRS ∼ 0.65 mg cm^{-2} LTFBB and PPS; electrochemical performance of D-LFP‖Gr full cells with LRS ∼ 1 mg cm^{-2} LTFBB and PPS; photos of 0.1 M TFBQ–LP57 electrolyte and LP57 at different viewing angles; galvanostatic rate performance of LP57 symmetrical cells; EIS spectra of 0.1 M TFBQ–LP57 and LP57 symmetrical cells, before and after the first 50 cycles; galvanostatic cycling performance of LP57 and 0.1 M TFBQ–LP57 symmetrical cells at 2 mA cm^{-2}/1 mA h cm^{-2}; calculation of Li content of LTFBB; theoretical atomic (C, O, F, and Li) weight of LTFBB; calculation of Li content of LTFBB after decomposition and the decomposition percentage of LTFBB during charging to 4.3 V. See DOI: https://doi.org/10.1039/d5ta09041e.

Acknowledgements

References

1 J. M. Tarascon and M. Armand, *Nature*, 2001, **414**, 359–367.
2 M. Armand and J. M. Tarascon, *Nature*, 2008, **451**, 652–657.
3 X. Chen, W. Li, C. Luo, H. Zhang, C. Gao, C. Sun, R. Wu, Y. Gong, P. Mu, Z. Lv and G. Cui, *Adv. Mater.*, 2025, **37**, e04360.
4 M. Li, H. Liu, Z. Cheng, J. He, H. Li, L. Zhang, T. Liu, X. Wang, P. Wang, Z. Liu and G. Cui, *Adv. Energy Mater.*, 2025, **15**, 2405766.
5 Y. Sun, H.-W. Lee, Z. W. Seh, N. Liu, J. Sun, Y. Li and Y. Cui, *Nat. Energy*, 2016, **1**, 15008.
6 Y. Sun, H.-W. Lee, Z. W. Seh, G. Zheng, J. Sun, Y. Li and Y. Cui, *Adv. Energy Mater.*, 2016, **6**, 1600154.
7 Y. Sun, H.-W. Lee, G. Zheng, Z. W. Seh, J. Sun, Y. Li and Y. Cui, *Nano Lett.*, 2016, **16**, 1497–1501.
8 J. Sun, L. Huang, G. Xu, S. Dong, C. Wang and G. Cui, *Mater. Today*, 2022, **58**, 110–118.
9 R. Zhan, X. Wang, Z. Chen, Z. W. Seh, L. Wang and Y. Sun, *Adv. Energy Mater.*, 2021, **11**, 2101565.
10 J. Choi, H. Jeong, J. Jang, A. R. Jeon, I. Kang, M. Kwon, J. Hong and M. Lee, *J. Am. Chem. Soc.*, 2021, **143**, 9169–9176.
11 Y. L. Cheah, V. Aravindan and S. Madhavi, *J. Electrochem. Soc.*, 2013, **160**, A1016.
12 Z. Liu, S. Ma, X. Mu, R. Li, G. Yin and P. Zuo, *ACS Appl. Mater. Interfaces*, 2021, **13**, 11985–11994.
13 P. Vanaphuti, L. Su and A. Manthiram, *Small Methods*, 2024, **8**, 2301159.

This journal is © The Royal Society of Chemistry 2026

J. Mater. Chem. A, 2026, **14**, 12314–12324 | 12323

14 M. Cao, Z. Liu, X. Zhang, L. Yang, S. Xu, S. Weng, S. Zhang, X. Li, Y. Li, T. Liu, Y. Gao, X. Wang, Z. Wang and L. Chen, *Adv. Funct. Mater.*, 2023, **33**, 2210032.

15 X.-Y. Yue, Y.-X. Yao, J. Zhang, S.-Y. Yang, Z. Li, C. Yan and Q. Zhang, *Adv. Mater.*, 2022, **34**, 2110337.

16 C. Li, H. Du, Y. Kang, Y. Zhao, Y. Tian, J. Wozny, J. Lu, T. Li, N. Tavajohi, M. Huang, B. Lan, F. Kang and B. Li, *Next Sustain.*, 2023, **1**, 100008.

17 B. Zhu, W. Zhang, Q. Wang, Y. Lai, J. Zheng, N. Wen and Z. Zhang, *Adv. Funct. Mater.*, 2024, **34**, 2315010.

18 G. Huang, J. Liang, X. Zhong, H. Liang, C. Cui, C. Zeng, S. Wang, M. Liao, Y. Shen, T. Zhai, Y. Ma and H. Li, *Nano Res.*, 2023, **16**, 3872–3878.

19 H. Park, T. Yoon, Y.-U. Kim, J. H. Ryu and S. M. Oh, *Electrochim. Acta*, 2013, **108**, 591–595.

20 B. Huang, T. Huang, L. Wan and A. Yu, *ACS Sustain. Chem. Eng.*, 2021, **9**, 648–657.

21 Z. Rao, J. Wu, B. He, W. Chen, H. Wang, Q. Fu and Y. Huang, *ACS Appl. Mater. Interfaces*, 2021, **13**, 38194–38201.

22 G. Lin, T. Meng, Y. Peng, P. Li and X. Hu, *Small Methods*, 2025, **9**, 2401133.

23 S. Chen, G. Wu, H. Jiang, J. Wang, T. Chen, C. Han, W. Wang, R. Yang, J. Zhao, Z. Tang, X. Gong, C. Li, M. Zhu, K. Zhang, Y. Xu, Y. Wang, Z. Hu, P. Chen, B. Wang, K. Zhang, Y. Xia, H. Peng and Y. Gao, *Nature*, 2025, **638**, 676–683.

24 K. Jun, L. Kaufman, W. Jung, B. Park, C. Jo, T. Yoo, D. Lee, B. Lee, B. D. McCloskey, H. Kim and G. Ceder, *Adv. Energy Mater.*, 2023, **13**, 2301132.

25 Y. Bie, J. Yang, J. Wang, J. Zhou and Y. Nuli, *Chem. Commun.*, 2017, **53**, 8324–8327.

26 Y. Sun, Y. Li, J. Sun, Y. Li, A. Pei and Y. Cui, *Energy Storage Mater.*, 2017, **6**, 119–124.

27 Q. Nie, W. Wan, Y. Mei, G. Qu, Z. Liu, C. Tie, J. Zhu, C. Ji, J. Chen, C. Wang and Y. Huang, *Adv. Funct. Mater.*, 2025, **35**, 2422034.

28 Y. Zhan, H. Yu, L. Ben, Y. Chen and X. Huang, *Electrochim. Acta*, 2017, **255**, 212–219.

29 Y. Fu, Y. Xie, L. Zeng and Z. Shi, *Surf. Interfaces*, 2023, **36**, 102610.

30 X. Wang, C. Liu, S. Zhang, H. Wang, R. Wang, Y. Li and J. Sun, *ACS Appl. Energy Mater.*, 2021, **4**, 5246–5254.

31 Q. Meng, M. Fan, X. Chang, H. Li, W.-P. Wang, Y.-H. Zhu, J. Wan, Y. Zhao, F. Wang, R. Wen, S. Xin and Y.-G. Guo, *Adv. Energy Mater.*, 2023, **13**, 2300507.

32 G. Liu, W. Wan, Q. Nie, C. Zhang, X. Chen, W. Lin, X. Wei, Y. Huang, J. Li and C. Wang, *Energy Environ. Sci.*, 2024, **17**, 1163–1174.

33 L. Du, G. Xu, Z. Zhang, X. Du, G. Kang, Y.-H. Zhang, B. Xie, X. Zhuang, J. Wang, T. Dong, C. Li, Q. Zhang, J. Ju, H. Zhang, S. Dong, G. Zhou and G. Cui, *ACS Energy Lett.*, 2025, **10**, 3941–3951.

34 M. Fan, Q. Meng, X. Chang, C.-F. Gu, X.-H. Meng, Y.-X. Yin, H. Li, L.-J. Wan and Y.-G. Guo, *Adv. Energy Mater.*, 2022, **12**, 2103630.

35 X. Chang, M. Fan, B. Yuan, W.-H. He, C.-F. Gu, C. Li, Q. Meng and Y.-G. Guo, *Angew. Chem., Int. Ed.*, 2024, **63**, e202406557.

36 N. Yao, F. Liu, A. Shao, R. Xue, Q. Jia, Y. Liu, H. Wang, X. Wang, Y. Zhang, M. Zhang, Z. Wang, Y. Li, J. Tang, X. Tang and Y. Ma, *Adv. Mater.*, 2024, **36**, 2408268.

37 M. K. Tran, M.-T. F. Rodrigues, K. Kato, G. Babu and P. M. Ajayan, *Nat. Energy*, 2019, **4**, 339–345.

38 M. Shan, C. Dang, K. Meng, Y. Cao, X. Zhu, J. Zhang, G. Xu and M. Zhu, *Mater. Today*, 2024, **73**, 130–150.

39 W. Wu, A. Wang, Q. Zhan, Z. Hu, W. Tang, L. Zhang and J. Luo, *Small*, 2023, **19**, 2301737.

40 D. Wang, Z. Zhang, B. Hong and Y. Lai, *Chem. Commun.*, 2019, **55**, 10737–10739.

41 P. Jeżowski, O. Crosnier, E. Deunf, P. Poizot, F. Béguin and T. Brousse, *Nat. Mater.*, 2018, **17**, 167–173.

42 T. Siodła, W. P. Oziminski, M. Hoffmann, H. Koroniak and T. M. Krygowski, *J. Org. Chem.*, 2014, **79**, 7321–7331.

43 J. T. Gozdalik, A. Adamczyk-Woźniak and A. Sporzyński, *Pure Appl. Chem.*, 2018, **90**, 677–702.

44 Q. Guo, H. Xu, X. Chu, X. Huang, M. Yu and X. Feng, *Chem. Soc. Rev.*, 2025, **54**, 4035–4086.

45 Z. Yao, J. Fu, Y. Liu, J. Hou, P. Vanaphuti, X. Ma, R. Zhang, Z. Yang and Y. Wang, *Sustain. Energy Fuels*, 2021, **5**, 5574–5580.

46 Y. Hu, L. Liu, J. Zhao, D. Zhang, J. Shen, F. Li, Y. Yang, Z. Liu, W. He, W. Zhao and J. Liu, *Batteries*, 2023, **9**, 322.

47 W. Li, H. Li, Z. Lu, L. Gan, L. Ke, T. Zhai and H. Zhou, *Energy Environ. Sci.*, 2015, **8**, 3629–3636.

48 W.-R. Liu, Z.-Z. Guo, W.-S. Young, D.-T. Shieh, H.-C. Wu, M.-H. Yang and N.-L. Wu, *J. Power Sources*, 2005, **140**, 139–144.

49 P. Liu, J. Wang, J. Hicks-Garner, E. Sherman, S. Soukiazian, M. Verbrugge, H. Tataria, J. Musser and P. Finamore, *J. Electrochem. Soc.*, 2010, **157**, A499.

50 J. Wang and X. Sun, *Energy Environ. Sci.*, 2015, **8**, 1110–1138.

51 M. R. Roberts, A. Madsen, C. Nicklin, J. Rawle, M. G. Palmer, J. R. Owen and A. L. Hector, *J. Phys. Chem. C*, 2014, **118**, 6548–6557.

52 D.-T. Ngo, R. Scipioni, S. B. Simonsen, P. S. Jørgensen and S. H. Jensen, *Int. J. Energy Res.*, 2016, **40**, 2022–2032.

53 G. Nichols, S. Byard, M. J. Bloxham, J. Botterill, N. J. Dawson, A. Dennis, V. Diart, N. C. North and J. D. Sherwood, *J. Pharm. Sci.*, 2002, **91**, 2103–2109.

54 R. Scipioni, P. S. Jørgensen, D.-T. Ngo, S. B. Simonsen, Z. Liu, K. J. Yakal-Kremski, H. Wang, J. Hjelm, P. Norby, S. A. Barnett and S. H. Jensen, *J. Power Sources*, 2016, **307**, 259–269.

55 J. Tan, J. Matz, P. Dong, J. Shen and M. Ye, *Adv. Energy Mater.*, 2021, **11**, 2100046.

56 Y. Wang, S. Zhang, Z. Chen, H. Zhang, F. Tian, J. Wang, Y. Zhu, G. Yang, Z. Li and G. Cui, *Adv. Mater.*, 2025, e14210.

57 A. Hussain, M. M. Mohamed, M. Faheem, Y. P. Hardianto, M. O. Aijaz, M. R. Karim and M. A. Aziz, *J. Polym. Sci.*, 2025, **63**, 3824–3836.

58 H. Widiyandari, O. A. Putra, A. Purwanto and Z. Abidin, *Mater. Today: Proc.*, 2021, **44**, 3245–3248.

12324 | *J. Mater. Chem. A*, 2026, **14**, 12314–12324

This journal is © The Royal Society of Chemistry 2026